POLITECNICO DI TORINO
Repository ISTITUZIONALE

Shape sensing methods: Review and experimental comparison on a wing-shaped plate

(Article begins on next page)

19 September 2024

SHAPE SENSING METHODS:
REVIEW AND EXPERIMENTAL COMPARISON
ON A WING-SHAPED PLATE

Priscilla Cerracchio, Marco Gherlone, Massimiliano Mattone

Politecnico di Torino – Department of Mechanical and Aerospace Engineering

Corso Duca degli Abruzzi 24, 10129 Turin, Italy

Abstract

Shape sensing, i.e., the reconstruction of the displacement field of a structure from some discrete surface strain measurements, is a fundamental capability for the structural health management of critical components. In this paper, a review of the shape sensing methodologies available in the open literature and of the different applications is provided. Then, for the first time, an experimental comparative study is presented among the main approaches in order to highlight their relative merits in presence of uncertainties affecting real applications. These approaches are, namely, the inverse Finite Element Method, the Modal Method and Ko's Displacement Theory. A brief description of these methods is followed by the presentation of the experimental test results. A cantilevered, wing-shaped aluminum plate is let deform under its own weight, leading to bending and twisting. Using the experimental strain measurements as input data, the deflection field of the plate is reconstructed using the three aforementioned approaches and compared with the actual measured deflection. The inverse Finite Element Method is proven to be slightly more accurate and particularly attractive because it is versatile with respect to the boundary conditions and it does not require any information about material properties and loading conditions.

Keywords: Shape sensing; inverse Finite Element Method; Experimental test; Surface strains

1. Introduction: a literature review

In the past few decades, increasing economical ad research efforts have been put into the development of *shape sensing* techniques, which enable the real-time evaluation of the displacement field from discrete strain measurements. The goal is the real-time evaluation of the strain and stress fields from the displacement field, which can be used by structural health monitoring systems or can be stored

as usage data [1-4]. The principal benefits are an increased safety and a more cost-efficient maintenance. In fact, the knowledge of the actual structural health state can allow a more accurate failure prediction and less maintenance to be performed based on actual data. Shape sensing is particularly important when applied loads are difficult to determine or measure, as for aerodynamic forces, vibrating excitations transmitted through junctions or impact loads.

Real-time shape sensing techniques play also a key role in the development of smart structures, such as those with morphing capabilities or structures with embedded antenna arrays that need feedback for actuation and control systems [5-7]. In addition, monitoring of the deformed shape is a vital aspect for control of large deployable frame structures that carry antennas [8-10]. For this kind of structures, accurate on-orbit shape estimation is required in order to increase communication quality.

For practical uses, shape sensing algorithms are almost exclusively based on strain measurements, as accurate and lightweight strain sensors are available in commerce, particularly Fiber Bragg Grating (FBG) sensors. The capability of using bonded or embedded FBG based strain sensing systems has been proved for monitoring airplane wings [11], spatial frame structures [8,12] and composite structures [13]. Traditional strain gauges are still employed in laboratory tests as their acquisition systems are simpler and less expensive. Very few works have been proposed in the literature, which make use of displacements or accelerations measured at a limited number of points [14-16].

As for the algorithms, a shape sensing methodology should be computationally fast, robust with respect to inherent errors in the strain measurements and general enough to model complex structural topologies under a wide range of loadings, boundary conditions, material systems and inertial/damping characteristics. Moreover, it is preferable that loading and/or material data are not required, especially if stress are not going to be evaluated, as these kind of information is difficult to obtain precisely outside of a laboratory environment.

Existing methodologies can mainly be grouped in the following four categories: (1) methods based on the numerical integration of experimental strains; (2) methods using global or piecewise continuous basis functions to approximate the displacement field; (3) methods employing Neural Networks (NN); and (4) methods based on a finite-element discrete variational principle. Very few examples of approaches obtained combining different methodologies can be found.

1.1. Methods based on integration of experimental strains

Most of the works which perform the integration of discretely measured strains, deal with beam problems and are founded on classical beam equations [5,11,17-21].

A remarkable effort has been performed by Ko and co-workers in developing and assessing a shape sensing strategy referred to as Ko's Displacement Theory and applicable to beams, wing-boxes and plates [11,17-20]. In [17] the key idea is proposed, i.e., the reconstruction of the deflection of a beam-like structure from double integration of axial strains measured by sensors (strain gages, optical fibers) aligned on a "sensing line" with a known distance from the neutral axis. For pure bending and sufficiently slender structures, classical Bernoulli-Euler assumptions are adopted. Transverse-shear induced additional deflection can be evaluated by knowing the shear force distribution along the axis of the structure. Similarly to bending deflection, it is possible to reconstruct the cross-section twist angle due to torsion by using strain gages oriented along the 45°-helical (principal) direction. Combined load cases with both bending and torsion can be analyzed. Examples on how to apply the approach are provided for simple beams with several boundary conditions and tapered wing-boxes. For the latter case, a two-line strain-sensing system on the top surface of the box is proposed. The deflection is evaluated at the two sensing lines only and the cross-sectional twist angle is computed by considering the difference in the deflection of the two lines. Moreover, the approach is also extended to plate structures by taking into account multiple parallel strain-sensing lines. In [18], further mathematical developments of the formulas presented in [17] are presented in order to make them easier to use. Moreover, a strategy to determine the distance from the sensing lines to the structure neutral axis is provided. New numerical examples are presented that scrutinize the application of Ko's Displacement Theory to wing-boxes: depth-tapered (unswept and swept), width-tapered unswept, and double-tapered unswept wing-boxes. The two sensing lines are located at the front and rear lower edges of each wing-box. In [11], the approach is applied to the doubly-tapered wing of the unmanned Ikhana aircraft. A high-fidelity FE model of the wing is used to provide both the strain data needed for input to the deformed shape reconstruction based on the Ko's Displacement Theory and the reference deflections and cross-sectional twist angles. In [19], an experimental assessment of the Ko's shape-sensing approach is presented. Ground tests (with a whiffletree arrangement) are performed on the wing of the Global Observer, a high-altitude long-endurance unmanned aerial vehicle. Strains are measured using optical fibers arranged in the usual two-line strain-sensing configuration (both on the upper and on the lower surface of the wing in order to evaluate the neutral axis location). A photogrammetry system is adopted to measure validation displacements. Further sensitivity analyses are documented in order to investigate the effect of noise in the strain data and uncertainties on the distance between strain stations, on the spanwise location of fibers on the wing and on the wing's cross-section thickness. In [20], a further experimental application of Ko's approach is presented (a cantilevered metallic plate with uniform cross-section thickness and width and with a 45° sweep angle).

Akl *et al.* used distributed strain sensors and a FEM approach to integrate the continuous measured strains [5]. The solution was then obtained in terms of nodal displacements. Non-linear strains were taken into account by adopting von Karman strain-displacement relationships. In [21], this approach was extended to the case of bi-dimensional structures.

1.2. Methods based on global or piecewise continuous basis functions

For the full-field estimation of the deformed shape, a number of works use global or piecewise continuous basis functions to approximate the strain field [7,26-37]. In particular, basis-function methods make use of an *a priori* set of spatial functions and proper weights to fit measured strains. The unknowns are represented by the weights, which are determined by discrete measurements of the strain. Then, the displacement field is obtained by means of strain-displacement relationships, while taking into account proper boundary conditions. If global basis functions are used, the number of strain measurements can be equal to or larger than the number of unknown weights and basis functions. When piecewise basis functions are employed, the number of required measurements is generally larger [22-24]. Concerning the choice of the basis functions, polynomials or polynomial splines have been employed. In most cases, the Bernoulli-Euler beam hypotheses or the Kirchhoff plate hypotheses were chosen to define the strain-displacement relationships, thus restricting the method to slender beams or thin plates. Todd and Vohra showed how the transverse shear effect can be included for the beam problem without requiring an independent measure of the corresponding shear strain [25].

When normal modes are employed as basis functions, the shape sensing algorithms are referred to as Modal Method (MM) or Modal Transformation Theory (MTT) [26-34]. Originally MTT was proposed simultaneously by Foss and Haugse [28] and by Pisoni *et al.* [33]. In these two early works the mode shapes were experimentally estimated. The experimental evaluation of the mode shapes can be onerous; on the other hand, it does not require any knowledge of the material properties. Other works based on the MTT adopted analytical [31] or FEM generated mode shapes [26,27,29,30,32,34]. Normally, the first few normal modes are used in the prediction algorithm, since they contribute most to the deformed shape. For high-frequency excitations, however, a large number of natural vibration modes is needed to improve the accuracy, thus requiring a large number of strain measurements [29]. Lively *et al.* showed that when only lower natural modes are used the results can be inaccurate due to the aliasing of higher structural modes [32]. To this purpose, they proposed to filter out higher frequencies contribution from measured strains by using low-pass filters or Kalman filters. Besides, Rapp *et al.* pointed out that, using a reduced number of strain sensors, unsatisfactory results are obtained, unless the sensor placement is optimized [34]. In [27], an approach is proposed to evaluate the relative importance

of mode shapes on the displacement field reconstruction. A modal cutoff criterion based on the strain energy related to each mode shape is presented.

1.3. Methods based on Neural Networks

In a different class of methods, various types of Neural Network (NN) were used to perform the shape reconstruction of frame structures [9,10]. However, a drawback of these methods is that their accuracy strongly relays on the choice of the load cases used for the training [9,10].

1.4. Methods based on a finite-element discrete variational principle

Particularly promising and versatile are the variational approaches, which employ different types of error functional and problem-dependent finite element approximations to solve the inverse problem of the full-field shape reconstruction [13,38-68].

Nishio *et al.* employed a weighted-least-squares formulation to reconstruct the deflection of a composite cantilevered plate with embedded optical fibers [13]. In this approach, compatibility between analytical and measured bending curvatures of the Kirchhoff plate theory is enforced in a weighted-least-squares sense. The weighting coefficients were adjusted in order to account for the inherent errors in the measured strain data. The weights were computed for a given data-acquisition apparatus, load case and test article, with the consequent difficulties in generalizing the procedure.

Shkarayev *et al.* used a least-squares algorithm which reconstructs the applied loading first and then leads to the displacements [38]. Particularly, the load is approximated by a polynomial whose coefficients are evaluated from the minimization of the least-squares error between estimated and measured strains.

Tessler and Spangler developed an inverse Finite Element Method (iFEM) for shear-deformable plate and shell structures [39,40]. The proposed methodology employs a variational principle based on a least-square functional, which is discretized by C^0-continuous *inverse* finite elements and that can accommodate arbitrarily positioned and oriented strain-sensor data. Minimization of the least-square functional with respect to nodal degrees of freedom enforces the compatibility between the measured strains and those interpolated within each inverse element. Since only strain-displacement relations are used in the formulation, both the static and the dynamic responses can be reconstructed without any a priori knowledge of material, inertial, loading, or damping structural properties. To model arbitrary plate and shell structures, Tessler and Spangler employed the First-order Shear Deformation Theory (FSDT) to develop a three-node inverse shell element called iMIN3 [41]. A further enhancement of the approach

is presented in [42] in order to allow shape sensing also when sparse strain data are available. An experimental assessment of the method can be found in [43,44], where the deformed shape of a slender beam is reconstructed by an iFEM shell model using FBG strain measurements. A further application of iFEM and iMIN3 can be found in [45]. A direct FE model of a real 30-ft half-span straight wing with two spars is used to provide both strain data and reference displacements. Several sensor configurations are tested and the effect of (numerical) noise on strain data is evaluated. In [46], iMIN3 is used to perform shape-sensing on a CFRP stiffened panel subjected to mechanical loads (static and dynamic) and, for the first time, thermal effects. The robustness of the method with respect to input errors (strain data) is also investigated. Further developments and applications of the iFEM approach for thin walled structures based on FSDT have been proposed by Kefal *et al.* [47-51]. In [47,48], a quadrilateral inverse shell element is developed and applied to the shape sensing of a cantilevered plate and of a stiffened plate under bending loads. The effect of sensor locations and number and of geometry discretization on the solution accuracy is also investigated. In [49,50], the quadrilateral inverse element is used to reconstruct the displacement field of a container ship under realistic loading conditions (sea waves). A similar study is proposed in [51] where the iFEM-based shape sensing is applied to a chemical tanker mid-ship.

The inverse Finite Element Method was specialized by Gherlone *et al.* for the shape sensing of truss, beam and frame structures instrumented with strain gauges [52,53]. A class of inverse beam elements based on Timoshenko beam theory has been developed. The kinematic assumptions include the axial, bending, torsional and transverse shear deformations of the beam that are taken into account in the iFEM least-square functional. Application of the beam-iFEM approach to several problems involving cantilevered beams and three-dimensional frame structures, undergoing static and dynamic responses, were presented [54-57]. In [58], the iFEM capability to predict deformed shape of beam structures was also experimentally demonstrated. Thin-walled circular beams in a cantilevered configuration have been subjected to both static and dynamic loads. The generated strains have been measured by using strain rosettes, displacements have been directly evaluated by using LVDTs (for static loads) and by double time integration of an accelerometer measurement (for dynamic loads).

Recently the iFEM formulation was extended by Cerracchio *et al.* first [59,60] and by Kefal *et al.* later [61,62] to multi-layered composite and sandwich structures by including the kinematic assumptions of the Refined Zigzag Theory [63]. The additional kinematic complexity of laminated structures (that can exhibit through-the-thickness piecewise (zigzag) distributions of in-plane displacements and strains) leads to the need of additional strains data to perform accurate shape-sensing analyses. Therefore, strains are evaluated on top and bottom laminate surfaces and at least at one internal layer interface and additional zigzag strain measures are included in the least-square functional [51,52]. A further

development of the least-square functional with higher-order strain measures taken into account is presented in [61,62].

Recently, an inverse non-linear membrane element has been proposed by Alioli *et al.* [64]. This new iFEM implementation is applied to the reconstruction of the deformed shape of a membrane under the action of static and unsteady aerodynamic loads. Both numerical and experimental results are presented.

In a series of four papers [65-68], Mainçon *et al.* proposed a regularized least-squares formulation that seeks the solution for displacements and loads simultaneously, requiring an a priori knowledge of a subset of applied loading and the material properties. The solution procedure minimizes a cost function consisting of unknown loads and differences between the measured and estimated strains; equilibrium constraints are added to the cost function by means of Tikhonov regularization. The number of unknowns is three times the number of the degrees-of-freedom in the finite element discretization. Importantly, the accuracy of the solution strongly depends on the choice of suitable weights; these are computed from a complex procedure involving the probability distributions of the unknown loads and measured data. In [67,68], sensitivity analyses were carried out for truss structures, investigating variations in the input data as well as the modeling errors.

1.5. Hybrid methods

Pak has recently proposed a "two-step" method for shape sensing [69] that can be considered as a hybrid approach since it takes advantage of both Ko's idea and of the Modal Method. In the "first step", strains are measured along sensing lines (instrumented with optical fibers), then fitted using a piecewise least-square fitting method together with the cubic spline technique and finally integrated twice to obtain deflections along the sensing lines. In the "second step", full-field structural deflections and slopes are recovered as a linear combination of mode shapes computed with a finite element model. The coefficients of this linear combination are obtained in order to fit the deflections provided by the first step. In [70], the two-step method by Pak is used to obtain velocities and accelerations by means of simple harmonic motion assumption.

1.6. Comparative studies

Few comparative studies on shape sensing methods are available in literature [10,69,71] and only consider two methods at a time. In [10], Mao *et al.* compared a NN approach with the modal basis-functions method. They observed that the modal approach is more accurate than the NN approach when the applied load is very different from the training load case set. On the other hand, the accuracy of the

Modal Method depends on the number of modes used. A comparison between Modal Method and Ko's Displacement Theory is performed in [71] where strain data are experimentally measured on a wing-like swept plate. The same plate, already used in [20], is further adopted as experimental test case in [69] where a comparison between the "two-step" method by Pak and Ko's Displacement Theory is presented.

1.7. Present effort

The present effort compares, for the first time, the three methods that represent the main families of shape sensing approaches: Ko's Displacement Theory [11], the Modal Method [27,29] and the iFEM for plate structures [41]. The Neural Network approach is not considered here as it does not seem promising due to the drawbacks already highlighted in some papers [9,10]. The three approaches are applied to the static reconstruction of the deformed shape of a cantilevered wing-shaped aluminum plate, instrumented with strain gauges. The plate is inspired by similar experiments presented in [20,69,71] (sweep angle) but it exhibits an additional geometric complexity (varying cross-section width) in order to better reproduce the structural response of a more complex wing structure. The aim is to test the accuracy of the three methods especially with respect to various sources of errors that inevitably afflict laboratory experiments as well as real applications. These errors include measurement ones but also uncertainty in strain gauges position, boundary conditions, and geometry.

The paper is organized as follows. In Section 2, a brief description of the shape sensing approaches under investigation is provided. Section 3 presents the experimental set-up (geometry, boundary conditions, measurement systems for both strains and deflections) and discusses the results obtained with the shape sensing methods. In Section 4, some conclusions are drawn on the performances and relative merits of the considered methodologies.

2. Review of inverse Finite Element Method, Modal Method and Ko's displacement theory

The shape sensing methods under investigation are here summarized and reviewed in order to set the computational framework for the comparative study.

2.1 inverse Finite Element Method

At first, the general formulation is presented and then the application to shear-deformable thin-walled structures is discussed [40-42].

A structural domain referred to a Cartesian coordinate system, $\mathbf{x} \equiv (x, y, z)$, can be discretized into one-, two- or three dimensional finite elements (in the following, denoted by the superscript e). The displacement field of the structure, $\left[u_x(\mathbf{x}), u_y(\mathbf{x}), u_z(\mathbf{x}) \right]^T$, can be expressed in terms of a vector of *kinematic variables*, $\mathbf{u}(\mathbf{x})$, consistent with a particular structural theory. The kinematic variables are approximated within each element e by using the shape functions

$$\mathbf{u}(\mathbf{x}) \approx \mathbf{u}^e = \mathbf{N}(\mathbf{x})\mathbf{q}^e \tag{1}$$

where $\mathbf{N}$ is the shape-function matrix and $\mathbf{q}^e$ is vector of the nodal degrees-of-freedom. Similarly, the strain field of the structure is fully defined by K independent *strain measures*, $\boldsymbol{\varepsilon} \equiv \{\varepsilon_k\}$ $(k = 1, ..., K)$, that can be easily related to the nodal degrees-of-freedom

$$\boldsymbol{\varepsilon}(\mathbf{u}^e) = \mathbf{B}(\mathbf{x})\mathbf{q}^e \tag{2}$$

where the matrix $\mathbf{B}$ contains the derivatives of the shape functions.

The iFEM provides a reconstruction of the kinematic variables by minimizing an error functional which can be defined, in each element, as the least-squares difference between the analytic strain measures, Eq. (2), and the corresponding experimental strain measures, $\boldsymbol{\varepsilon}^\varepsilon \equiv \{\varepsilon_k^\varepsilon\}$ $(k = 1, ..., K)$, measured at n discrete locations by in-situ suitable strain sensors

$$\Phi^e(\mathbf{u}^e) = \left\| \boldsymbol{\varepsilon}(\mathbf{u}^e) - \boldsymbol{\varepsilon}^\varepsilon \right\|^2 \tag{3}$$

The element least-squares difference, Φ^e, can be expressed as follows [42]

$$\Phi^e(\mathbf{u}^e) \equiv \sum_{k=1}^{K} \lambda_k^e w_k^e \Phi_k^e \tag{4}$$

where:

- Φ_k^e, corresponding to the k-th strain measure component, is calculated over the n discrete measurement locations

$$\Phi_k^e \equiv \frac{1}{n} \sum_{i=1}^{n} \left[\varepsilon_{k(i)}(\mathbf{u}^e) - \varepsilon_{k(i)}^{\varepsilon} \right]^2 \quad (k = 1,...K) \tag{5}$$

- w_k^e is a dimensional coefficient, which guarantees that the terms of the summation in Eq. (4) have the same physical units;

- λ_k^e is a dimensionless coefficient that can assume different values in order to enforce a stronger or weaker correlation between measured and analytic strain-measures.

The dimensionless coefficients λ_k^e play a fundamental role in the iFEM since they make the approach applicable also to those cases when experimental strain measures are known with an insufficient degree of accuracy. Small values of the corresponding λ_k^e coefficient can be adopted in these cases. When some elements have not experimental strain data (even only some of the K components), another strategy is possible and will be discussed below for the case of shear-deformable thin-walled structures.

The element functional $\Phi^e(\mathbf{u}^e)$ is then minimized with respect to the unknown nodal degrees-of-freedom, $\mathbf{q}^e$, yielding the element matrix equation

$$\frac{\partial \Phi^e(\mathbf{u}^e)}{\partial \mathbf{q}^e} = \mathbf{0} \quad \Rightarrow \quad \mathbf{A}^e \mathbf{q}^e = \mathbf{b}^e \tag{6}$$

Upon performing the coordinate transformation from each element local system to the global one and assembling the contribution of all the elements, the global system of equations is obtained

$$\mathbf{A}\mathbf{q} = \mathbf{b} \tag{7}$$

where the matrix $\mathbf{A}$ depends on the strain sensors locations, whereas the vector $\mathbf{b}$ also depends on the experimental strain data. By introducing the geometric-displacement boundary conditions that prevent rigid-body motion, the unknown nodal degrees-of-freedom are computed from Eq. (7) as $\mathbf{q} = \mathbf{A}^{-1}\mathbf{b}$.

Since only strain-displacement relations are discretized by the iFEM formulation, the approach does not require the knowledge of any material properties, damping properties or the applied loading. Thus, it is applicable for both static and dynamic loading conditions. In particular, $\mathbf{A}$ is inverted only once and $\mathbf{b}$ is updated at each strain-data acquisition increment (for dynamic problems).

The iFEM has been applied to shear-deformable thin-walled structures using the First-order Shear Deformable Theory as structural theory [40,41]. A plate of thickness $2h$ is referred to the Cartesian coordinate system with (x, y) identifying the mid-plane (Figure 1). The components of the displacement vector are expressed by FSDT in terms of the kinematic variables as follows

$$\begin{aligned} u_x(\mathbf{x}) &= u + z\theta_y \\ u_y(\mathbf{x}) &= v + z\theta_x \\ u_z(\mathbf{x}) &= w \end{aligned} \tag{8}$$

FIGURE 1

The kinematic variables are $\mathbf{u} \equiv \left[u,\ v,\ w,\ \theta_x,\ \theta_y \right]^T$: u and v are the average uniform displacements in the x and y directions, respectively; θ_x and θ_y are the rotations of the normal about the negative x and positive y axes, respectively; and w is the average transverse deflection.

A three-node inverse plate element, labeled *iMIN3*, is formulated [41]. The kinematic variables are interpolated within each element using C^0-continous anisoparametric shape functions in order to suppress shear locking. The deflection is interpolated with a quadratic polynomial, whereas the other four kinematic variables vary linearly over the element. The resulting element has five degrees-of-freedom in each node (three displacements and two bending rotations).

The strain field of FSDT is characterized by eight strain measures [40], $\{\varepsilon_k\} = [\mathbf{e}, \mathbf{k}, \mathbf{g}]^T$ (K=8)

$$\begin{aligned} \mathbf{e} &= \left\{ u_{,x},\ v_{,y},\ \theta_{x,y} + \theta_{y,x} \right\}^T &&= \left\{ \varepsilon_1,\ \varepsilon_2,\ \varepsilon_3 \right\}^T \\ \mathbf{k} &= \left\{ \theta_{y,x},\ \theta_{x,y},\ \theta_{x,x} + \theta_{y,y} \right\}^T &&= \left\{ \varepsilon_4,\ \varepsilon_5,\ \varepsilon_6 \right\}^T \\ \mathbf{g} &= \left\{ w_{,x} + \theta_y,\ w_{,y} + \theta_x \right\}^T &&= \left\{ \varepsilon_7,\ \varepsilon_8 \right\}^T \end{aligned} \tag{9}$$

where $\mathbf{e}$ are the *membrane strain measures*, $\mathbf{k}$ are the *bending curvatures* and $\mathbf{g}$ are the *transverse-shear strain measures*. The dimensional coefficients corresponding to the K=8 terms of the least-square functional are as follows [41,42]: $w_k^e = 1$ for k=1,2,3,7,8 and $w_k^e = (2h)^2$ for k=4,5,6.

In-plane strain measures can be experimentally evaluated from strain-sensor data [41]. In particular, membrane and bending strain measures can be evaluated at discrete locations $(x, y)_i$ $(i = 1, ..., n)$ from surface strains measured on the top (+) and bottom (−) surfaces (see Figure 2) as

$$\mathbf{e}_i^\varepsilon = \frac{1}{2}\left(\left\{\begin{array}{c}\varepsilon_{xx}^+\\\varepsilon_{yy}^+\\\gamma_{xy}^+\end{array}\right\}_i + \left\{\begin{array}{c}\varepsilon_{xx}^-\\\varepsilon_{yy}^-\\\gamma_{xy}^-\end{array}\right\}_i\right), \quad \boldsymbol{\kappa}_i^\varepsilon = \frac{1}{2h}\left(\left\{\begin{array}{c}\varepsilon_{xx}^+\\\varepsilon_{yy}^+\\\gamma_{xy}^+\end{array}\right\}_i - \left\{\begin{array}{c}\varepsilon_{xx}^-\\\varepsilon_{yy}^-\\\gamma_{xy}^-\end{array}\right\}_i\right) \tag{10}$$

where $\left[\varepsilon_{xx}^+,\varepsilon_{yy}^+,\gamma_{xy}^+\right]_i^T$ and $\left[\varepsilon_{xx}^-,\varepsilon_{yy}^-,\gamma_{xy}^-\right]_i^T$ are the in-plane surface strains measured at $[(x,y)_i,+h]$ and $[(x,y)_i,-h]$, respectively (Figure 2).

FIGURE 2

By using the present kinematic interpolations, the membrane and bending strain measures are constant within each inverse element, therefore one measurement point per element is sufficient and it would be optimally located at the element centroid. Transverse-shear strain measures, $\{\varepsilon_k\} = \mathbf{g} \ (k=7,8)$, cannot be evaluated experimentally. Therefore, the corresponding contributions to the functional can not be written in the form of Eq. (5) and are consequently expressed as

$$\Phi_k^e \equiv \int_{A^e} \varepsilon_{k(i)}^2 \left(\mathbf{u}^e\right) dA \quad (k=7,8) \tag{11}$$

where A^e is the element area.

When only few strain sensors are available, some elements may not have any strain data. In this case, Eq. (11) is used instead of Eq. (5) for all the terms in the functional $(k=1,...,8)$. For these elements, the dimensionless coefficients $\lambda_k^e \ (k=1,...,8)$ assume small values (10^{-3}–10^{-6}) compared to the values used for the elements that possess strain data [42]. This penalization strategy can be selective, i.e., small values of λ_k^e can be used in some elements for the only strain components that are not experimentally measured. Since no experimental evaluation is possible for the transverse-shear strain measures, $\lambda_k^e \ (k=7,8)$ should always be attributed small values.

2.2 Modal Method

The Modal Method for shape sensing is based on the knowledge of the mode shapes of the structure under investigation. Let us consider that a finite element model is used to provide such information [27]. Given a FE discretization of the structure, for example a plate (as in the current case), the deflection at the *j*-th node can be expressed in terms of *M* mode shapes, i.e.,

$$w_j \cong \sum_{i=1}^{M} a_i \phi_i\left(x_j, y_j\right) \quad \Leftrightarrow \quad \mathbf{w} = \mathbf{\Phi a} \tag{12}$$

where ϕ_i are the mode shapes (collected in the modal matrix $\mathbf{\Phi}$) and a_i ($i = 1,..,M$) are the unknown modal coordinates (collected in the vector $\mathbf{a}$). Applying the strain-displacement relations, it is possible to express the vector of surface strains at the measurement points, $\mathbf{\varepsilon}$, as follows

$$\mathbf{\varepsilon} = \mathbf{\Psi a} \tag{13}$$

where the matrix $\mathbf{\Psi}$ contains the strain mode shapes (the i-th column of $\mathbf{\Psi}$, ε_i, contains the measured strains corresponding to the i-th mode shape, ϕ_i). Eq. (13) can be solved for $\mathbf{a}$ by using the Moore-Penrose pseudo inverse matrix

$$\mathbf{a} = (\mathbf{\Psi}^T \cdot \mathbf{\Psi})^{-1} \mathbf{\Psi}^T \cdot \mathbf{\varepsilon} \tag{14}$$

Substituting Eq. (14) into Eq. (12), yields

$$\mathbf{w} = \mathbf{\Phi} \left(\mathbf{\Psi}^T \cdot \mathbf{\Psi} \right)^{-1} \mathbf{\Psi}^T \cdot \mathbf{\varepsilon} \tag{15}$$

2.3 Ko's displacement theory

The Ko's displacement theory [11] has been developed to evaluate the deflection of an aircraft wing along a line of strain sensors. Let us consider the wing-shaped cantilevered structure represented in Figure 3. The plate belongs to the (x,y) plane.

FIGURE 3

The dashed line, referred to the coordinate s, represents a path along which longitudinal surface strains ε_{ss} are measured. There are $(N+1)$ locations where strains are measured, s_i $(i = 0,1,...,N)$, with s_0 and s_N corresponding to the clamped and tip end of the sensing line, respectively. The measured strains are denoted by $\varepsilon_i \equiv \varepsilon_{ss}(s_i)$. Following the assumptions of the Bernoulli-Euler's theory for pure bending, it is possible to relate the axial strain to the second derivative of the deflection (Figure 3)

$$\varepsilon_{ss}(s) = -z w_{,ss}(s) \tag{16}$$

where z is the distance between the strain sensor and the neutral axis. Ko's approach has been formulated in [11] (i) for the case of uniformly distributed measurement locations, i.e., $s_i - s_{i-1} = const. \left(i = 1, 2, ..., N\right)$ and (ii) with a distance from the neutral axis than can be different at the different locations. For the current application, we need to generalize the approach by relaxing condition (i) and assuming that the considered plate has constant thickness $2h$ (i.e., all the strains are measured at the same distance from the neutral axis, $z = -h$ if the top surface is instrumented). From Eq. (5) we obtain

$$w_{,ss}(s) = \frac{\varepsilon_{ss}(s)}{h} \tag{17}$$

The longitudinal strain is measured at the $(N+1)$ discrete locations and it is assumed to be linear between any sensor and the next one

$$\varepsilon_{ss}(s) = \varepsilon_{i-1} + \frac{\left(\varepsilon_i - \varepsilon_{i-1}\right)}{\left(s_i - s_{i-1}\right)}\left(s - s_{i-1}\right), \quad s_{i-1} \leq s \leq s_i \quad \left(i = 1, 2, ... N\right) \tag{18}$$

Double integration of Eq. (17) with the strain expressed by Eq. (18) in each interval, taking into account the clamped end boundary conditions ($w_0 = w(s = s_0) = 0$ and $\theta_0 = w_{,s}(s = s_0) = 0$) and the continuity of deflection and rotation at each measurement point, provides the following expression for the deflection [72]

$$w_i = \frac{1}{6h}\left[\sum_{j=1}^{i}\left(2\varepsilon_{j-1} + \varepsilon_j\right)\left(s_j - s_{j-1}\right)^2 + 3\sum_{k=1}^{i-1}\left(\varepsilon_{k-1} + \varepsilon_k\right)\left(s_k - s_{k-1}\right)\left(s_i - s_k\right)\right] \quad \left(i = 1, 2, ..., N\right) \tag{19}$$

For practical reasons, it is difficult to mount strain sensors at the clamped and at the tip end. Nevertheless, ε_0 can be inferred by applying a polynomial extrapolation based on the strain measurements closest to the clamp whereas ε_N is assumed to be zero.

Ko's displacement theory provides an evaluation of the deflection at the same locations where strains are measured whereas both iFEM and the Modal Method allow reconstructing the displacement field over the whole structure.

3.   Experimental results

The iFEM, Modal Method and Ko's displacement theory have been applied to the shape sensing of an aluminum cantilever plate. The whole experimental activity (material characterization included) has been conducted at the LAQ-AERMEC laboratory of the Mechanical and Aerospace Engineering Department of the Politecnico di Torino. For sake of simplicity, the following acronyms will be used: "iFEM" for the inverse Finite Element Method, "MM" for the Modal Method and "Ko" for the Ko's displacement theory.

3.1 Geometry and material properties of the plate

The plate has a wing-like shape with span $L = 994$ mm, root chord $c_R = 378$ mm, tip chord $c_T = 120$ mm, leading-edge sweep angle $\Lambda = 28°$ and thickness $2h = 3$ mm (Figure 4(a)). The plate is tested in a cantilevered configuration under the effect of its own weight (Figures 4(a), 4(b)).

FIGURE 4(a)
FIGURE 4(b)

The material is a 7075 aluminum alloy with Young's modulus $E = 72017$ MPa, Poisson's ratio $v = 0.325$ and mass density $\rho = 2.7$ g/cm^3. The material properties have been measured through a set of tensile tests on small specimens and have been employed only in the FE model used to evaluate the mode shapes.

3.2 Strain sensors location and mesh for the shape sensing methods

Strains are experimentally measured in some discrete locations on the top surface using linear strain gages. The experimental test is settled up so that the same experimental measures can be used in all of the three methods. The aim of the present paper is to assess and to compare three shape-sensing techniques within a laboratory framework, i.e., with input data experimentally measured on a real plate. Since the search for the minimum number (and optimal location) of strain sensors would be outside the scope of the present effort, the three shape sensing approaches have been applied with as many strain input data as possible. The available acquisition system can manage up to 44 linear strain measurements.

The distribution of the sensors is firstly inspired by the application of Ko's method to a wing structure [11]. Strain sensors are located along two measurement lines running from the clamped to the tip end

and subdividing each chord (with length $c(y)$) into three segments with lengths $c(y)/6$, $4c(y)/6$ and $c(y)/6$ (Figure 5(a)). Considering that the iFEM approach provides more accurate results if strains are measured at the centroid of the inverse triangular elements, the inverse mesh is constructed in such a way that the centroids of some elements belong to the sensing lines (Figure 5(b)). There are 132 inverse elements, 44 sensorized with a linear strain gauge (22 for each measurement line). The Modal Method requires the knowledge of some mode shapes data in order to construct the matrices $\mathbf{\Phi}$ and $\mathbf{\Psi}$. A modal analysis has been conducted with MSC/NASTRAN using a high-fidelity FE direct model. The mesh consists of 1188 QUAD elements (36 for each set of 4 inverse elements grouped to mesh a quadrilateral subdomain) with some nodes corresponding to the 44 measurement points (Figure 5(c))[1].

FIGURE 5(a)

FIGURE 5(b)

FIGURE 5(c)

The first 6 numerical mode shapes (and corresponding natural frequencies) are shown in Figure 6 (color contours indicate deflection levels).

FIGURE 6

The optimal number of mode shapes, M=6, has been determined by means of a convergence study. The direct FE model (Figure 5(c)) has been used to provide the data for the shape sensing based on the Modal Method: the mode shapes and the surface strains at the selected 44 locations as input data, the displacement field as a reference result. Figure 7 shows the RMS percent error between the reconstructed and the reference deflection field as a function of M

$$\%e_{RMS} \equiv 100 \times \sqrt{\frac{1}{n}\sum_{i=1}^{n}\left(\frac{w_i^{MM} - w_i^{NASTRAN}}{w_{max}^{NASTRAN}}\right)^2} \tag{20}$$

where the index i ranges over the n nodes of the mesh (Figure 5(c)). For $M \geq 6$ no appreciable error reduction is experienced. On the other hand, the use of non-necessary additional higher-order mode

---

[1] A convergence analysis has been performed on the first 20 natural frequencies and corresponding mode shapes. The mesh with 1188 QUAD elements (Mesh A) has been refined up to 19008 QUAD elements (Mesh B, 16 elements for any of the original ones) leading to negligible changes of the results. The variation on the 20th natural frequency is 0.8% and the Modal Assurance Criterion value calculated for the 20th mode shape of Mesh A and Mesh B is 0.992. For this reason, results obtained using Mesh A can be considered accurate.

shapes to model a structural response under simple static loading conditions can lead to an over-fitting condition. This is a possible explanation for the RMS behavior around the 19th mode (Figure 7).

FIGURE 7

Figure 8 shows the plate with the 44 linear strain gages (HBM® 1-LY1x-10/120) located along the two measurement lines.

FIGURE 8

3.3 Experimental set-up, procedure and results

The plate is clamped at one end between three couples of iron blocks locked together by eighteen bolted connections (see Figures 9(a)). The clamped area of the plate is pierced in correspondence of the bolted connections (see Figure 8). A zoomed view of some strain gages is provided in Figure 9(b).

FIGURE 9(a)
FIGURE 9(b)

Before starting the test, the plate is kept horizontally in the undeformed configuration by a granite support placed on an hydraulic lift table cart (Figure 10). The support is accurately aligned with the clamping.

FIGURE 10

When the support is removed, the plate is deflected under its own weight; global torsion is also observed since the plate reproduces the bending-torsion coupled response of a swept wing (Figure 11).

FIGURE 11(a)
FIGURE 11(b)

Strains are recorded using a HBM® – MGC Plus acquisition system. Figure 12 shows the strain distribution along the two measurement lines.

FIGURE 12

The plate deflection is experimentally measured by using two cameras and digital image correlation [73]. A set of targets (white crosses on a black background) are placed along the trailing and leading edges of the plate, at a distance of 5 mm one from another (Figure 13).

FIGURE 13

Images of the undeformed and deformed plate are acquired by using two digital cameras, one located in front of the leading edge and the other in front of the trailing edge (see Figure 14).

FIGURE 14

The images are post-processed by using MATLAB R2007a routines to extract the position of the targets from the pictures and then to compute the deflection field by difference:
- the images are transformed into black/white binary images by using an appropriate threshold value;
- the targets are identified in the images by cross-correlating the discrete Fourier transforms of the pictures with a reference image of the target (the target positions are given by local maxima of the cross-correlation function);
- the plate deflection (units of pixel) is obtained at each target location by comparing the position of the target in the pictures of the undeformed and deformed plate (Figure 15);
- pixel/millimeter conversion is performed by placing an object of known size in the picture frame (this also gives the resolution of the displacement measurements, which is of about 0.1 mm).

FIGURE 15(a)
FIGURE 15(b)

3.4 Shape sensing based on the experimental strains

The reconstruction of the displacement field of the wing-shaped plate through iFEM has been carried out by using the iMIN3 mesh represented in Figure 5(b). Referring to Eq. (4), for the transverse shear terms and for the elements that do not possess any strain data, a small value (10^{-4}) is used for λ_k^e ($k=1,\ldots,8$). Figures 16 and 17 compare the iFEM results with the deflection measured via image correlation for the trailing edge (TE) and leading edge (LE), respectively. Half-span of the plate (close

to the tip end) has been monitored using two cameras (Figure 14). The iFEM evaluated deflection and the image correlation measure exhibit slightly higher differences at the margins of the monitored zone. This discrepancy may be reasonably attributed to an aberration effect, which could be corrected by using telecentric lenses.

FIGURE 16

FIGURE 17

Experimentally measured strain data have been also used to feed the shape-sensing analysis via Modal Method and Ko's displacement theory. The accuracy of the deformed shape obtained using the three considered shape sensing approaches can be evaluated by introducing the percent difference of the reconstructed deflection, w^{rec}, with respect to the experimentally measured one, w^{exp},

$$\%\mathrm{Diff}\left(w(j)\right) = 100 \times \left[\frac{w^{rec}(j) - w^{exp}(j)}{\max\left(w^{exp}(j)\right)} \right] \tag{21}$$

where $\max\left(w^{exp}(j)\right)$ is the maximum measured deflection (at the tip of the trailing edge) and (j) is an index ranging over the locations of the leading or trailing edges where the deflection is evaluated.

The shape sensing approach based on Ko's displacement theory provides deflections along the same lines where strains are measured (w_1^{Ko} and w_2^{Ko} for lines 1 and 2, respectively, refer to Figure 5(a)) whereas deflections are experimentally measured along the trailing and leading edges. Therefore, in order to evaluate the percent difference in a consistent manner, w_{TE}^{Ko} and w_{LE}^{Ko} must be evaluated. Since this issue is not addressed in papers by Ko, the following assumption is made: the wing cross-section undergoes a rigid translation and rotation (Figure 18).

FIGURE 18

Given the location of the sensing lines along the cross-section chord $c(y)$ (Figure 18), the following relations can be obtained easily

$$w_{TE}^{Ko} = \frac{-w_1^{Ko} + 5w_2^{Ko}}{4}$$
$$w_{LE}^{Ko} = \frac{5w_1^{Ko} - w_2^{Ko}}{4}$$

(22)

Moreover, since the strains at the clamped end of the sensor lines are also required by the Ko's approach, these values have been obtained through a linear extrapolation based on the two strains measurements that are closer to the clamped edge of the plate.

Figure 19 shows the percent difference of the deflections predicted with the shape sensing methods investigated. iFEM appears to be globally more accurate as compared with the other two methods along the trailing edge (the percent difference ranges from -1.5% to 2%, whereas it reaches 4% at the tip for Ko and is close to -3% at $y/L = 0.4$ for the MM). The Modal Method is more accurate close to the tip of the leading edge (where iFEM and Ko's approach exhibit similar performances, with a tip percent difference around 4%). iFEM provides a better deflection reconstruction along the internal span of the leading edge.

FIGURE 19(a)
FIGURE 19(b)

4. Conclusions

The paper presents a review of the currently available methodologies to perform shape sensing, i.e., the reconstruction of the displacement field of a structure from the knowledge of strains measured in some discrete locations. The main families of approaches to shape sensing are identified as the inverse Finite Element Method (iFEM), the Modal Method (MM) and Ko's displacement theory (Ko). The methods are briefly described in order to set the numerical framework for the subsequent comparative study.

A wing-shaped plate has been tested in an experimental laboratory framework in order to provide both the strain data for the shape-sensing analyses and the deflection of the trailing and leading edges used to assess the accuracy of the three approaches. The plate is let deform under its own weight, strains are measured using linear strain gauges and deflection is measured through an optical method.

iFEM is shown to be globally more accurate in reconstructing the trailing edge deformed shape, whereas iFEM and MM accuracy is comparable along the leading edge. The percent difference between the reconstructed deflection and the one experimentally measured is lower than 4% for all the three approaches, thus demonstrating that they are reasonably comparable in terms of accuracy even in

presence of unavoidable uncertainties related to the experimental framework. Nevertheless, it has to be recalled that this accuracy is achieved by MM through a preliminary FE modal analysis that requires the knowledge of the structure material properties. On the other hand, Ko is able to directly provide deflection at the same locations where strains are measured. iFEM is much more flexible (no limitations on the boundary conditions and on the locations where displacement is reconstructed) and does not require data on the material properties and on the applied loads. iFEM is therefore advisable as an accurate and efficient approach to shape sensing. Further investigations and comparative studies will focus on numerical and experimental shape sensing of more complex structures (wing-boxes).

5. References

[1] Baroth E, Powers WT, Fox J, Prosser B, Pallix J, Schweikard K, Zakrajsek J. IVHM (Integrated Vehicle Health Management) techniques for future space vehicles. In Proceedings of the 37th AIAA/ASME/SAE/ASEE Joint Propulsion Conference Exhibit. Salt Lake City. AIAA 2001-3523. 2001.

[2] Integrated Vehicle Health Management (IVHM). NASA Website. https://www.nasa.gov/centers/ames/research/humaninspace/humansinspace-ivhm.html (Last accessed: December 2017)

[3] Paris DE, Trevino LC, Watson MD. A framework for integration of IVHM technologies for intelligent integration for vehicle management. In Proceedings of the 2005 IEEE Aerospace Conference. Big Sky. 2005.

[4] Tessler A. Structural analysis methods for Structural Health Management of future aerospace vehicles. NASA/TM-2007-214871. 2007.

[5] Akl W, Poh S, Baz A. Wireless and distributed sensing of the shape of morphing structures. Sensors Actuators A 2007;140:94-102.

[6] Hopkins MA, Truss JM, Lockyer AJ, Alt K, Kinslow R, Kudva JN. Smart skin conformal load bearing antenna and other smart structures developments. In Proceedintgs of the 38th AIAA/ASME/ASCE/AHS/ASC, Structures, Structural Dynamics and Materials Conference. Kissimmee. 1997.

[7] Yin W, Fu T, Liu J, Leng J. Structural shape sensing for variable camber wing using FBG sensors. In Proceedings of the SPIE 7292, Sensors and Smart Structures Technologies for Civil, Mechanical, and Aerospace Systems. San Diego. 2009.

[8]   Arritt B, Murphey T, Dumm HP, Pollard E, Klimcak C. Demonstration of the use of fiber-optics, with Integrated Fiber-Bragg Gratings, for shape determination of large deployable structures. In Proceedings of the 48th AIAA/ASME/ASCE/AHS/ASC Structures, Structural Dynamics, and Materials Conference. Honolulu. AIAA 2007-2006. 2007.

[9]   Bruno R, Toomarian N, Salama M. Shape estimation from incomplete measurements: a neural-net approach. Smart Materials and Structures 1994;3:92-97.

[10]   Mao Z, Todd M. Comparison of shape reconstruction strategies in a complex flexible structure. In Proceedings of the SPIE 6932, Sensors and Smart Structures Technologies for Civil, Mechanical, and Aerospace Systems. San Diego. 2008.

[11]   Ko WL, Richards WL, Fleischer VT. Applications of the Ko displacement theory to the deformed shape predictions of the doubly-tapered Ikhana wing. NASA/TP-2009-214652. 2009.

[12]   Blandino J R, Duncan RG, Nuckels MC, Cadogan D. Three-dimensional shape sensing for inflatable booms. In Proceedings of the 46th AIAA/ASME/ASCE/AHS/ASC Structures, Structural Dynamics & Materials Conference. Austin. AIAA 2005-1807. 2005.

[13]   Nishio M, Mizutani T, Takeda N. Structural shape reconstruction with consideration of the reliability of distributed strain data from a Brillouin-scattering-based optical fiber sensor. Smart Materials and Structures 2010;19:1-14.

[14]   Maia NMM, Silva JMM, Ribeiro AMR. The transmissibility concept in multi-degree-of-freedom systems. Mechanical Systems and Signal Processing 2001;15:129-137.

[15]   He J, Guan X, Liu Y. Structural response reconstruction based on empirical mode decomposition in time domain. Mechanical Systems and Signal Processing 2012;28:348-366.

[16]   Chipman C, Avitabile P. Expansion of real time operating data for improved visualization. In Proceedings of the 26th International Modal Analysis Conference. Orlando. 2008.

[17]   Ko WL, Richards WL, Fleischer VT. Displacement theories for in-flight deformed shape predictions of aerospace structures. NASA/TP-2007-214612. 2007.

[18]   Ko WL, Fleischer VT. Further development of Ko displacement theory for deformed shape predictions of nonuniform aerospace structures. NASA/TP-2009-214643. 2009.

[19]   Jutte CV, Ko WL, Stephens CA, Bakalyar JA, Richards WL, Parker AR. Deformed shape calculation of a full-scale wing using fiber optic strain data from a ground loads test. NASA/TP-2011-215975. 2011.

[20] Bakalyar JA, Jutte CV. Validation tests of fiber optic strain-based operational shape and load measurements. In Proceedings of the 20th AIAA/ASME/AHS Adaptive Structures Conference. Honolulu. 2012.

[21] Smoker B, Baz A. Monitoring the bending and twist of morphing structures. In Proceedings of the SPIE 6932, Sensors and Smart Structures Technologies for Civil, Mechanical, and Aerospace Systems. San Diego. 2008.

[22] Glaser R, Caccese V, Shahinpoor M. Shape monitoring of a beam structure from measured strain or curvature. Experimental Mechanics 2012;52:591-606.

[23] Gopinathan M, Pajunen GA, Neelakanta PS, Arockaisamy M. Recursive estimation of displacement and velocity in a cantilever beam using a measured set of distributed strain data. Journal of Intelligent Material Systems and Structures 1995;6:537-549.

[24] Kirby III GC, Lim TW, Weber R, Bosse A, Povich C, Fisher S. Strain-based shape estimation algorithms for a cantilever beam. In Proceedings of the SPIE 3041, Smart Structures and Materials 1997: Smart Structures and Integrated Systems. San Diego. 1997.

[25] Todd MD, Vohra ST. Shear deformation correction to transverse shape reconstruction from distributed strain measurements. Journal of Sound and Vibration 1999;225:581-594.

[26] Bang HJ, Ko SW, Jang MS, Kim KI. Shape estimation and health monitoring of wind turbine tower using a FBG sensor array. In Proceedings of the IEEE Instrumentation and Measurement Technology Conference. Graz. 2012.

[27] Bogert PB, Haugse ED, Gehrki RE. Structural shape identification from experimental strains using a modal transformation technique. In Proceedings of the 44th AIAA/ASME/ASCE/AHS Structures, Structural Dynamics and Materials Conference. Norfolk. AIAA 2003-1626. 2003.

[28] Foss G, Haugse E. Using modal test results to develop strain to displacement transformations. In Proceedings of the 13th International Conference on Modal Analysis. Nashville. 1995.

[29] Kang LH, Kim DK, Han JH. Estimation of dynamic structural displacements using fiber Bragg grating strain sensors. Journal of Sound and Vibration 2007;305:534-542.

[30] Kim HI, Kang LH, Han JH. Shape estimation with distributed fiber Bragg grating sensors for rotating structures. Smart Materials and Structures 2011;20:1-11.

[31] Li CJ, Ulsoy GA. High-precision measurement of tool-tip displacement using strain gauges in precision flexible line boring. Mechanical Systems and Signal Processing 1999;13:531-546.

[32] Lively PS, Atalla MJ, Hagood NW. Investigation of filtering techniques applied to the dynamic shape estimation problem. Smart Materials and Structures 2001;10:264-272.

[33] Pisoni AC, Santolini C, Hauf DE, Dubowsky S. Displacements in a vibrating body by strain gauge measurements. In Proceedings of the 13th International Conference on Modal Analysis. Nashville. 1995.

[34] Rapp S, Kang LH, Han JH, Mueller UC, Baier H. Displacement field estimation for a two-dimensional structure using fiber Bragg grating sensors. Smart Materials and Structures 2009;18:025006.

[35] Davis MA, Kersey AD, Sirkis J, Friebele EJ. Shape and vibration mode sensing using a fiber optic Bragg grating array. Smart Materials and Structures 1996;5:759-765.

[36] Jones RT, Bellemore DG, Berkoff TA, Sirkis JS, Davis MA, Putnam MA, Friebele EJ, Kersey AD. Determination of cantilever plate shapes using wavelength division multiplexed fiber Bragg grating sensors and a least-squares strain-fitting algorithm. Smart Materials and Structures 1998;7:178-188.

[37] Kim NS, Cho NS. Estimating deflection of a simple beam model using fiber optic Bragg-grating sensors. Experimental Mechanics 2004;44:433-439.

[38] Shkarayev S, Krashantisa R, Tessler A. An inverse interpolation method utilizing in-flight strain measurements for determining loads and structural response of aerospace vehicles. In Proceedings of the 3rd International Workshop on Structural Health Monitoring. Stanford. 2001.

[39] Tessler A, Spangler JL. A variational principal for reconstruction of elastic deformation of shear deformable plates and shells. NASA/TM-2003-212445. 2003.

[40] Tessler A, Spangler JL. A least-squares variational method for full-field reconstruction of elastic deformations in shear-deformable plates and shells. Computer Methods in Applied Mechanics and Engineering 2005;194:327-339.

[41] Tessler A, Spangler JL. Inverse FEM for full-field reconstruction of elastic deformations in shear deformable plates and shells. In Proceedings of the 2nd European Workshop on Structural Health Monitoring. Munich. 2004.

[42] Tessler A, Spangler JL, Mattone M, Gherlone M, Di Sciuva M. Real-time characterization of aerospace structures using onboard strain measurement technologies and inverse Finite Element Method. In Proceedings of the 8th International Workshop on Structural Health Monitoring. Stanford. 2011.

[43] Quach CC, Vazquez SL, Tessler A, Moore JP, Cooper EG, Spangler JL. Structural anomaly detection using fiber optic sensors and inverse Finite Element Method. In Proceedings of the AIAA Guidance, Navigation, and Control Conference and Exhibit. San Francisco. 2005.

[44] Vazquez SL, Tessler A, Quach CC, Cooper EG, Parks J, Spangler JL. Structural health monitoring using high-density fiber optic strain sensor and inverse Finite Element Methods. NASA/TM-2005-213761. 2005.

[45] Miller EJ, Manalo R, Tessler A. Full-field reconstruction of structural deformations and loads from measured strain data on a wing test article using the inverse Finite Element Method. NASA/TM-2016-219407. 2016.

[46] Cerracchio P, Gherlone M, Tessler A. Real-time displacement monitoring of a composite stiffened panel subjected to mechanical and thermal loads. Meccanica 2015;50:2487–2496.

[47] Kefal A, Oterkus E. Structural health monitoring of marine structures by using inverse Finite Element Method. Proceedings of the 5th International Conference on Marine Structures. Southampton. 2015.

[48] Kefal A, Oterkus E, Tessler A, Spangler JL. A quadrilateral inverse-shell element with drilling degrees of freedom for shape sensing and structural health monitoring. Engineering Science and Technology, an International Journal 2016;19:1299-1313.

[49] Kefal A, Oterkus E. Shape- and stress-sensing of a container ship by using inverse Finite Element Method. Proceedings of the International Conference on Smart Ship Technology. London. 2016.

[50] Kefal A, Oterkus E. Displacement and stress monitoring of a Panamax containership using inverse Finite Element Method. Ocean Engineering 2016;119:16–29.

[51] Kefal A, Oterkus E. Displacement and stress monitoring of a chemical tanker based on inverse Finite Element Method. Ocean Engineering 2016;112:33–46.

[52] Gherlone M. Beam inverse finite element formulation. LAQ Report. Politecnico di Torino. 2008

[53] Gherlone M, Cerracchio P, Mattone M, Di Sciuva M, Tessler A. Shape sensing of 3D frame structures using an inverse Finite Element Method. International Journal of Solids and Structures 2012;49:3100-3112.

[54] Cerracchio P, Gherlone M, Mattone M, Di Sciuva M, Tessler A. Shape sensing of three-dimensional frame structures using the inverse Finite Element Method. In Proceedings of the 5th European Workshop on Structural Health Monitoring. Sorrento. 2010.

[55] Gherlone M, Cerracchio P, Mattone M, Di Sciuva M, Tessler A. Dynamic shape reconstruction of three-dimensional frame structures using the inverse Finite Element Method. In Proceedings of the 3rd ECCOMAS Thematic Conference on Computational Methods in Structural Dynamics and Earthquake Engineering. Corfù. 2011.

[56] Gherlone M, Cerracchio P, Mattone M, Di Sciuva M, Tessler A. Dynamic shape reconstruction of three-dimensional frame structures using the inverse Finite Element Method. NASA/TP-2011-217315. 2011.

[57] Gherlone M, Cerracchio P, Mattone M, Di Sciuva M, Tessler A. Beam shape sensing using inverse Finite Element Method: theory and experimental validation. In Proceedings of the 8th International Workshop on Structural Health Monitoring. Stanford. 2011.

[58] Gherlone M, Cerracchio P, Mattone M, Di Sciuva M, Tessler A. Inverse Finite Element Method for beam shape sensing: theoretical framework and experimental validation. Smart Materials and Structures 2014;23:045027.

[59] Cerracchio P, Gherlone M, Di Sciuva M, Tessler A. Shape and stress sensing of multilayered composite and sandwich structures using an inverse finite element method. In Proceedings of the 5th International Conference on Computational Methods for Coupled Problems in Science and Engineering. Ibiza. 2013.

[60] Cerracchio P, Gherlone M, Di Sciuva M, Tessler A. A novel approach for displacement and stress monitoring of sandwich structures based on the inverse Finite Element Method. Composite Structures 2015;127:69-76.

[61] Kefal A, Tessler A, Oterkus E. An enhanced inverse Finite Element Method for displacement and stress monitoring of multilayered composite and sandwich structures. Composite Structures 2017;179:514-540.

[62] Kefal A, Yildiz M. Modeling of sensor placement strategy for shape sensing and structural health monitoring of a wing-shaped sandwich panel using inverse Finite Element Method. Sensors 2017;17(12).

[63] Tessler A, Di Sciuva M, Gherlone M. A consistent refinement of first-order shear-deformation theory for laminated composite and sandwich plates using improved zigzag kinematics. Journal of Mechanics of Materials and Structures 2010;5:341-367.

[64] Alioli M, Masarati P, Morandini M, Carpenter T, Osterberg NB, Albertani R. Membrane shape and load reconstruction from measurements using inverse Finite Element analysis. AIAA Journal 2017;55:297-308.

[65] Mainçon P. Inverse FEM I: Load and response estimates from measurements. In Proceedings of the 2nd International Conference on Structural Engineering, Mechanics and Computation. Cape Town. 2004.

[66] Mainçon P. Inverse FEM II: Dynamic and non-linear problems. In Proceedings of the 2nd International Conference on Structural Engineering, Mechanics and Computation. Cape Town. 2004.

[67] Maree AJ, Mainçon P. Inverse FEM III: Influence of measurement data availability. In Proceedings of the 2nd International Conference on Structural Engineering, Mechanics and Computation. Cape Town. 2004.

[68] Barnardo C, Mainçon P. Inverse FEM IV: Influence of modeling error. In Proceedings of the 2nd International Conference on Structural Engineering, Mechanics and Computation. Cape Town. 2004.

[69] Pak C. Wing shape sensing from measured strain. AIAA Journal 2016;54:1064-1073.

[70] Pak C, Truax RA. Acceleration and velocity sensing from measured strain. AIAA Infotech @ Aerospace, AIAA SciTech Forum. San Diego. 2016.

[71] Derkevorkian A, Masri SF, Alvarenga J, Boussalis H, Bakalyar J, Richards L. Strain-based deformation shape-estimation algorithm for control and monitoring applications. AIAA Journal 2013;51:2231-2240.

[72] Cerracchio P. Inverse methods for health monitoring and shape sensing of aerospace structures. PhD Thesis. Politecnico di Torino. 2014.

[73] Schreier H, Orteu JJ, Sutton MA. Image correlation for shape, motion and deformation measurements. New York: Springer, 2009.

Figure captions

Figure 1. Plate notation.

Figure 2. Strain gauge instrumentation.

Figure 3. Wing-shaped plate referred to the Cartesian coordinate system (x,y,z). (N+1) strain sensors are aligned along a measurement line (referred to the coordinate s) and provide axial strains ε_i.

Figure 4. Wing-shaped plate: (a) geometry and boundary conditions, (b) real plate (the green area corresponds to the geometry described in (a), the red area is used to clamp the plate).

Figure 5. Strain-sensors location and grid points for the considered shape sensing methods: (a) measurement lines for Ko's method, (b) tria inverse mesh for iFEM (44 linear strain gages – SG – are located along the measurement lines of Figure 5(a) and correspond to the centroid of 44 inverse elements), (c) QUAD MSC/NASTRAN direct mesh used to provide mode shapes for the Modal Method.

Figure 6. First six mode shapes and corresponding natural frequencies (MSC/NASTRAN solution, Figure 5(c)).

Figure 7. Modal Method: RMS percent error (Eq. (20)) as a function of the number of mode shapes.

Figure 8. Aluminum wing-shaped plate instrumented with 44 strain gages.

Figure 9. Aluminum wing-shaped plate experiment: (a) clamping system and (b) detail of the strain-gage instrumentation.

Figure 10. Aluminum wing-shaped plate mounted on the test bed.

Figure 11. Aluminum wing-shaped plate deflected under its own weight: (a) top view and (b) lateral view.

Figure 12. Axial strains measured on the top surface of the wing-shaped plate.

Figure 13. Detail of the leading edge with targets for the displacement measurements by using digital image correlation.

Figure 14. Set-up for the experimental measurement of the plate deflection along the leading and trailing edges.

Figure 15. Images of the trailing edge of the plate in the (a) undeformed and (b) deformed configuration.

Figure 16. Trailing edge deflection of the wing-shaped plate: iFEM reconstruction vs experimental measurements. Data-points obtained with the iFEM approach corresponds to the nodes of the inverse mesh belonging to the trailing edge (Figure 5(b)).

**Figure 17.** Leading edge deflection of the wing-shaped plate: iFEM reconstruction vs experimental measurements.

Figure 18. Evaluation of deflections along the leading and the trailing edge for Ko's Displacement Theory.
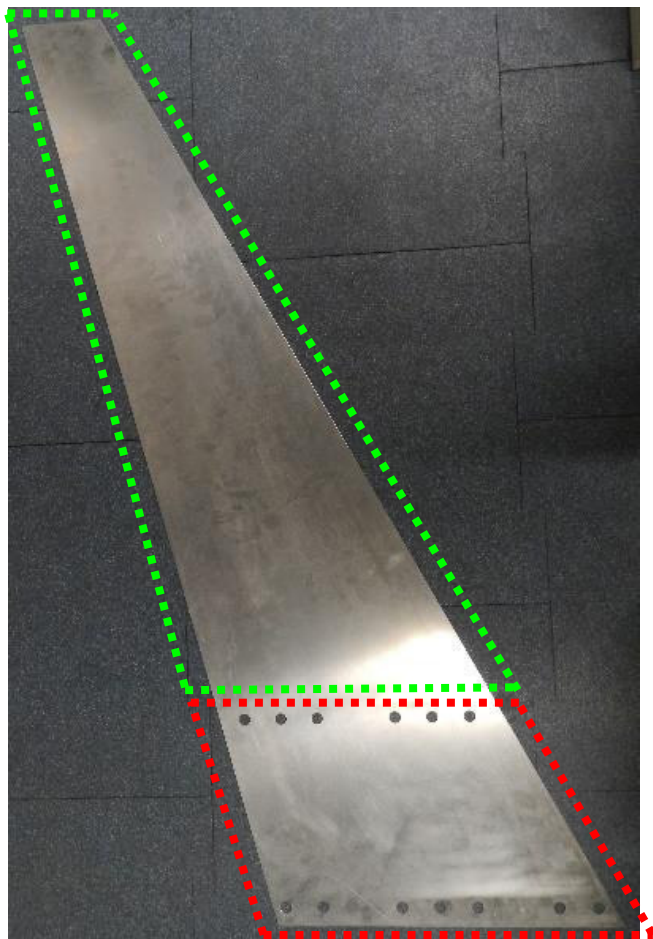
Figure 19. Percent difference in the predicted deflections using iFEM, Ko's Displacement Theory and Modal Method: (a) trailing edge deflection and (b) leading edge deflection.
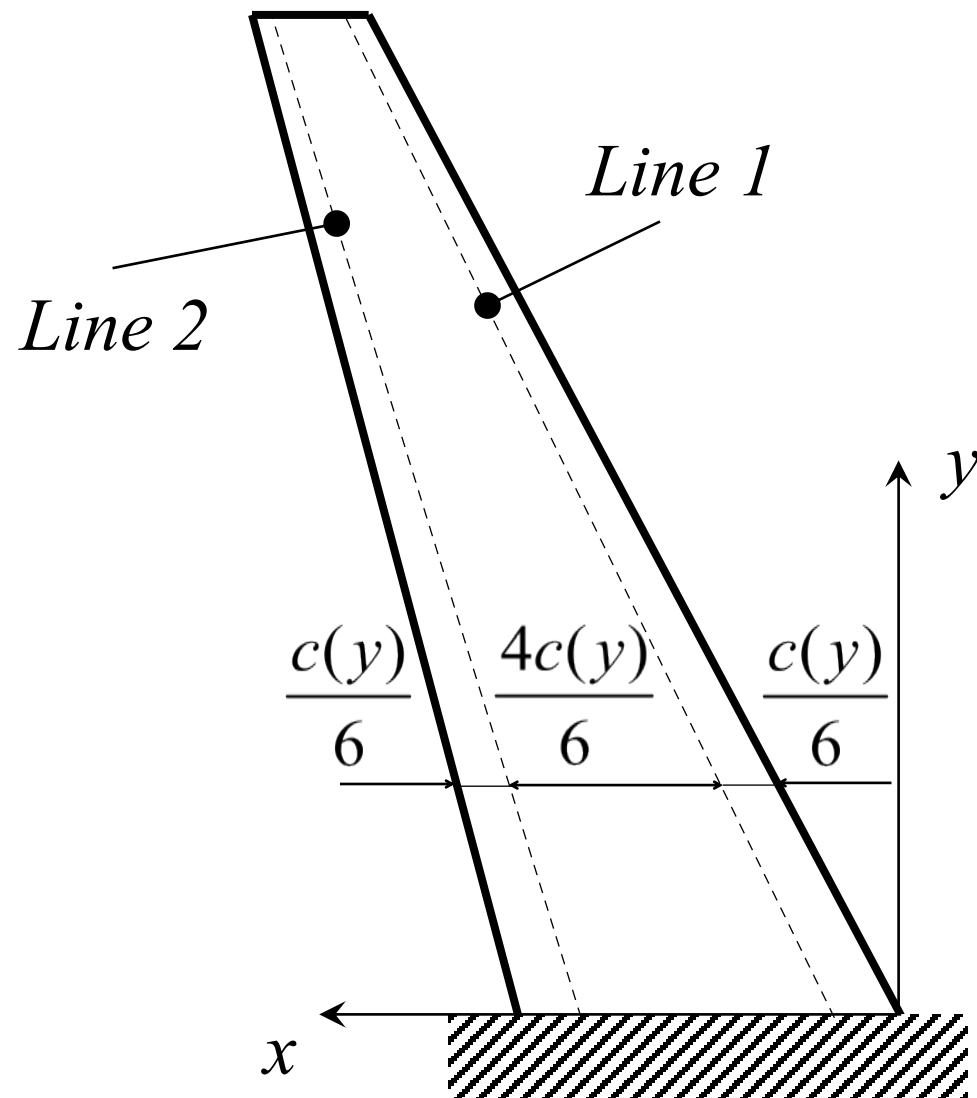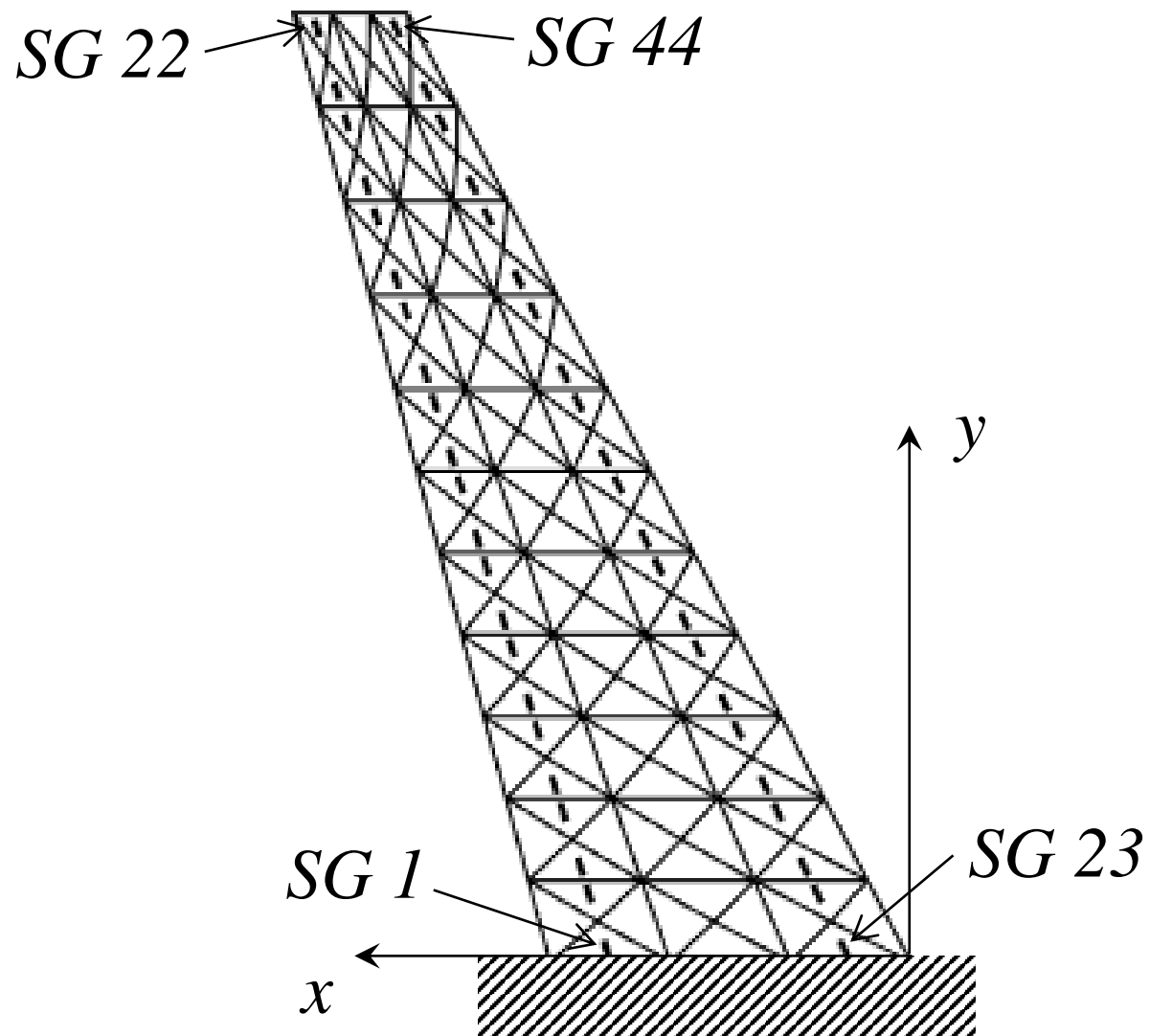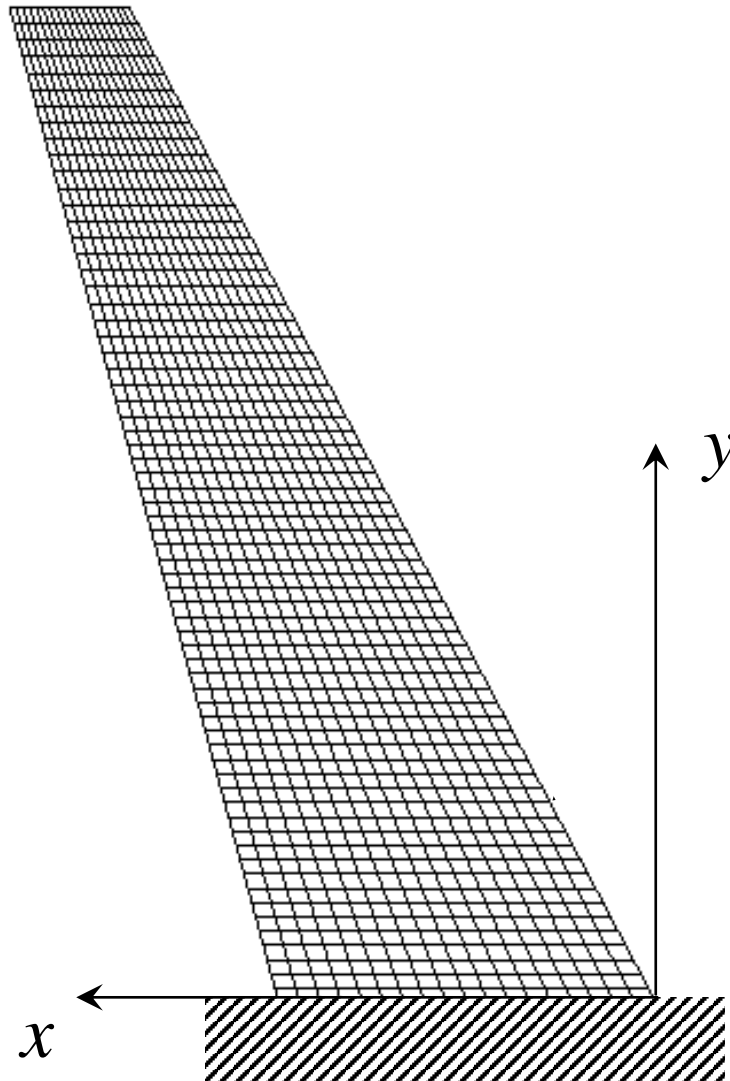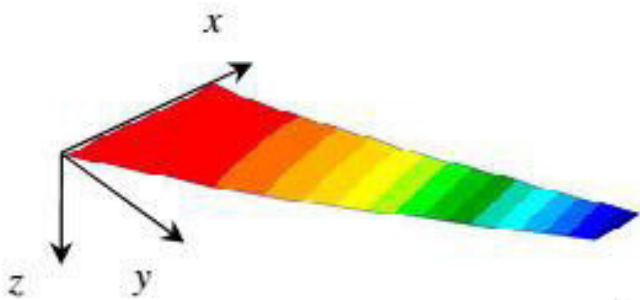
c_T
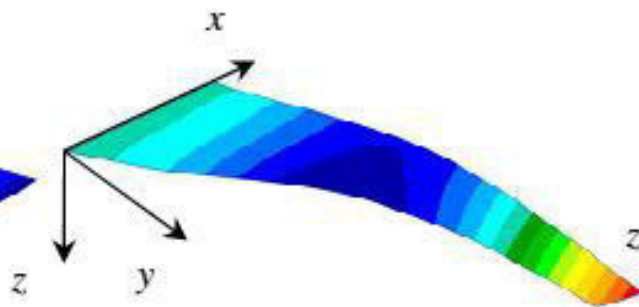
Trailing edge

Leading edge

L

Λ

c_R

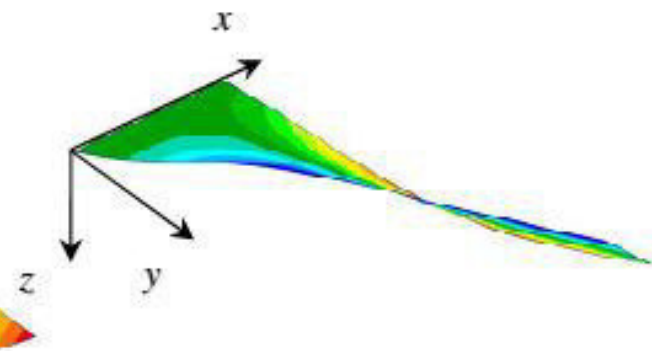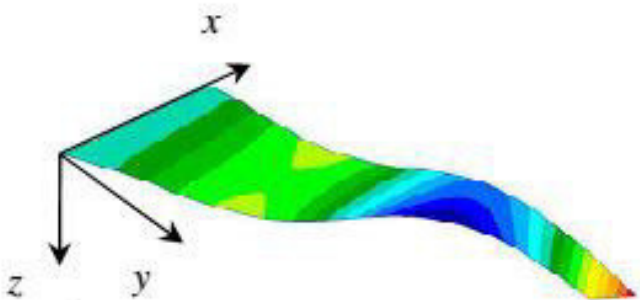SG 22   SG 44

SG 1   SG 23

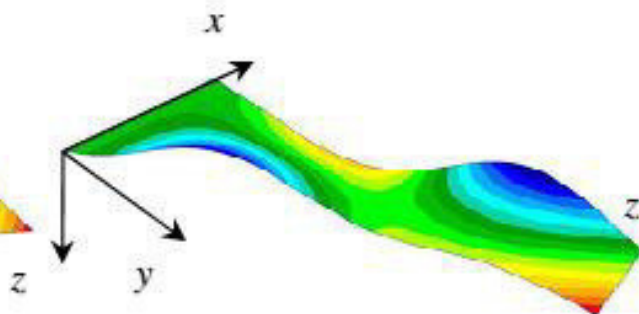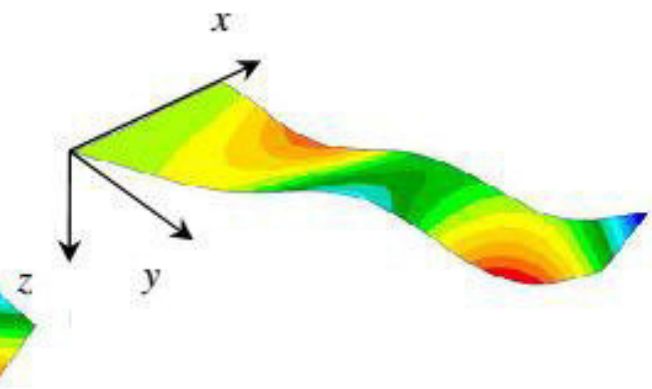y

x
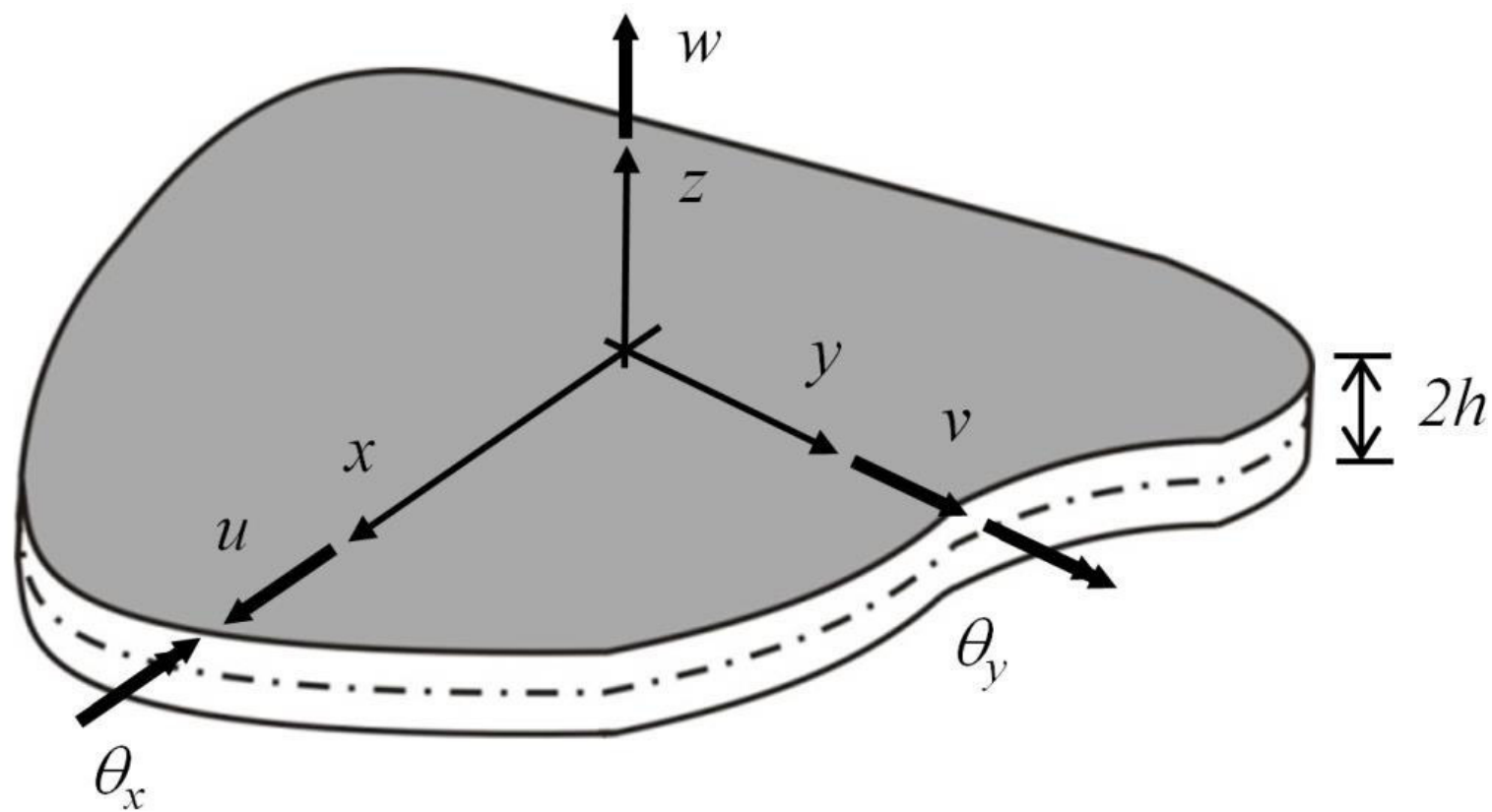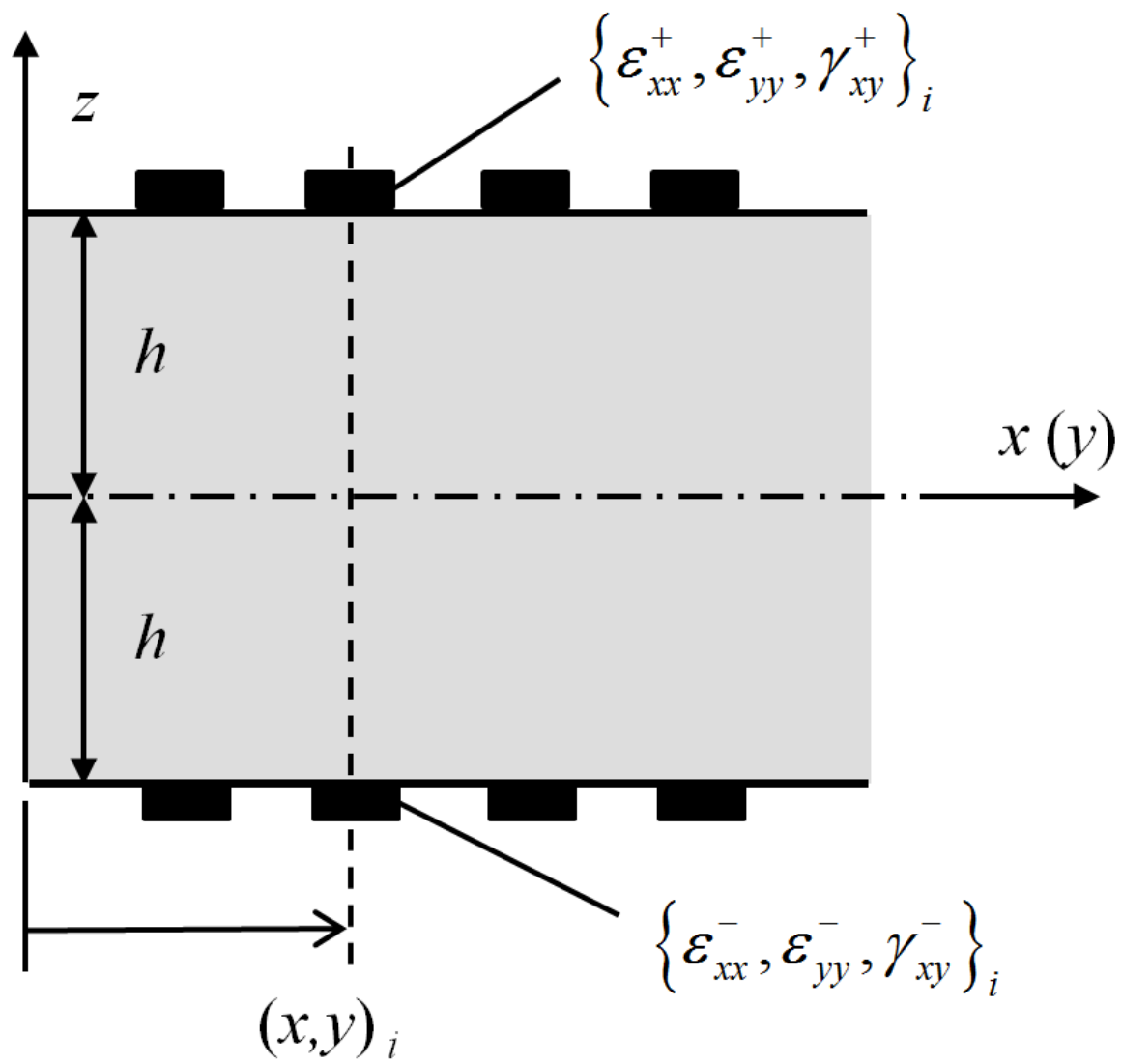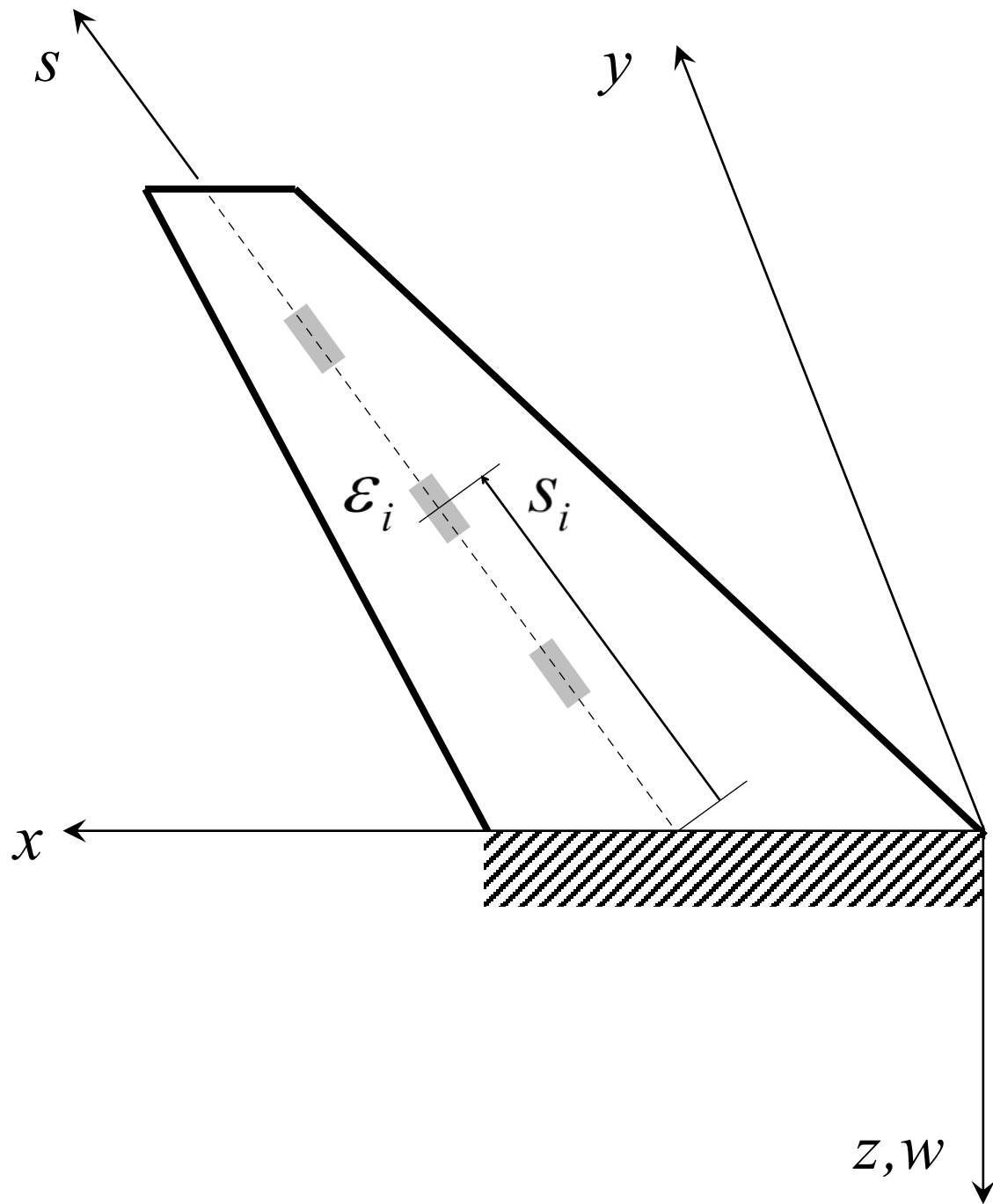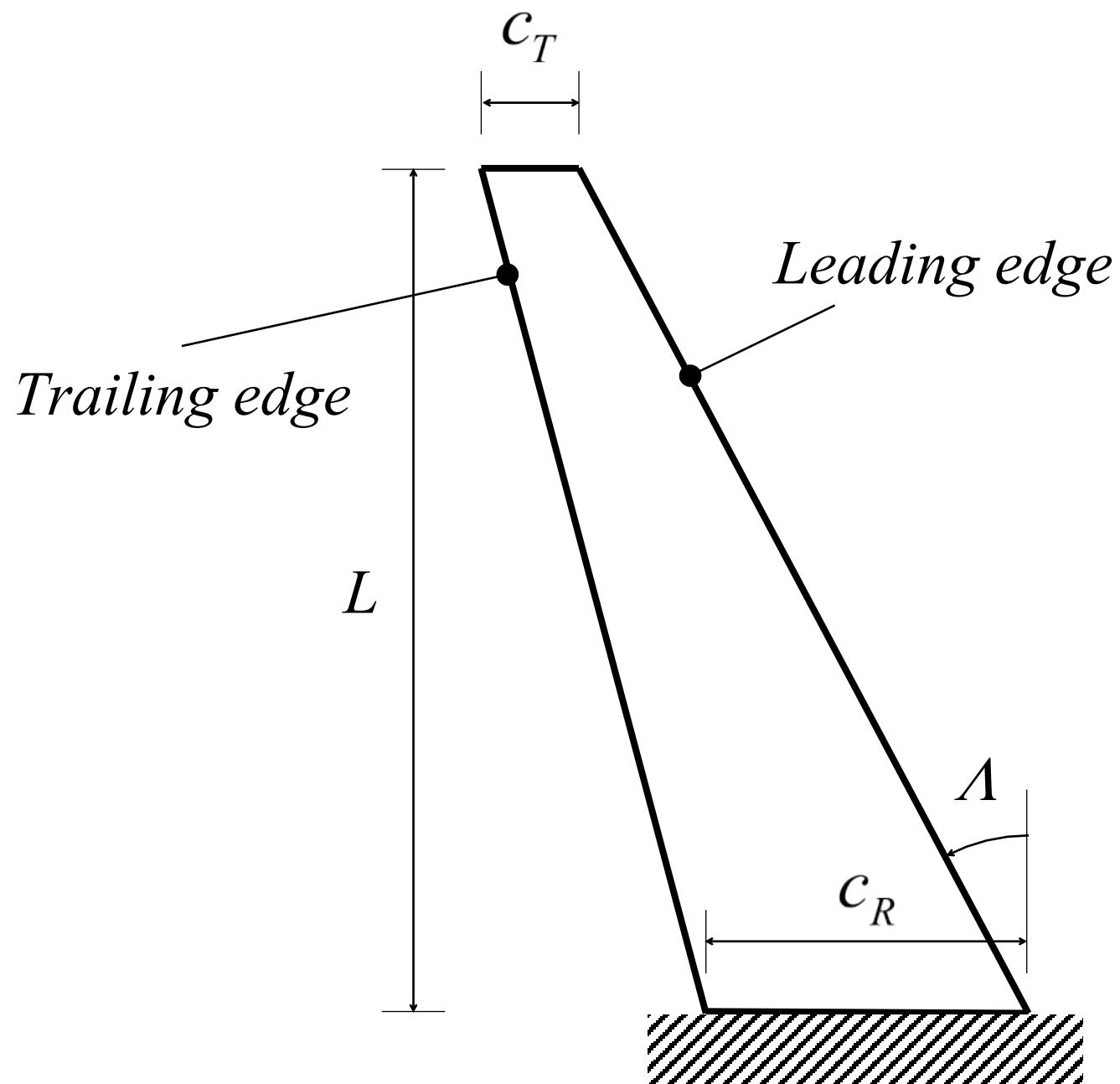
1st mode
(3 Hz)

2nd mode
(16 Hz)

3rd mode
(31 Hz)

4th mode
(42 Hz)

5th mode
(73 Hz)

6th mode
(82 Hz)